Silicon Based $Bi_{0.9}La_{0.1}FeO_3$ Ferroelectric Tunnel Junction Memristor for Convolutional Neural Networks Application

Gongjie Liu[1], Wei Wang[1], Zhenqiang Guo[1], Xiaotong Jia[1], Zhen Zhao[1], Zhenyu Zhou[1], Jiangzhen Niu[1], Guojun Duan[1] and Xiaobing Yan[1]*

* Corresponding author

Address correspondence to Xiaobing Yan, yanxiaobing@ime.ac.cn

[1]Key Laboratory of brain-like neuromorphic devices and Systems of Hebei Province, College of Electron and Information Engineering, Hebei University, Baoding 071002, P. R. China.

Keywords: Ferroelectric memristor, Artificial synapses, Image Processing, Convolutional neural networks.
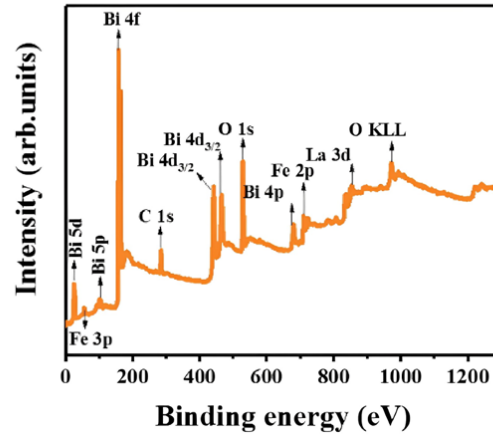
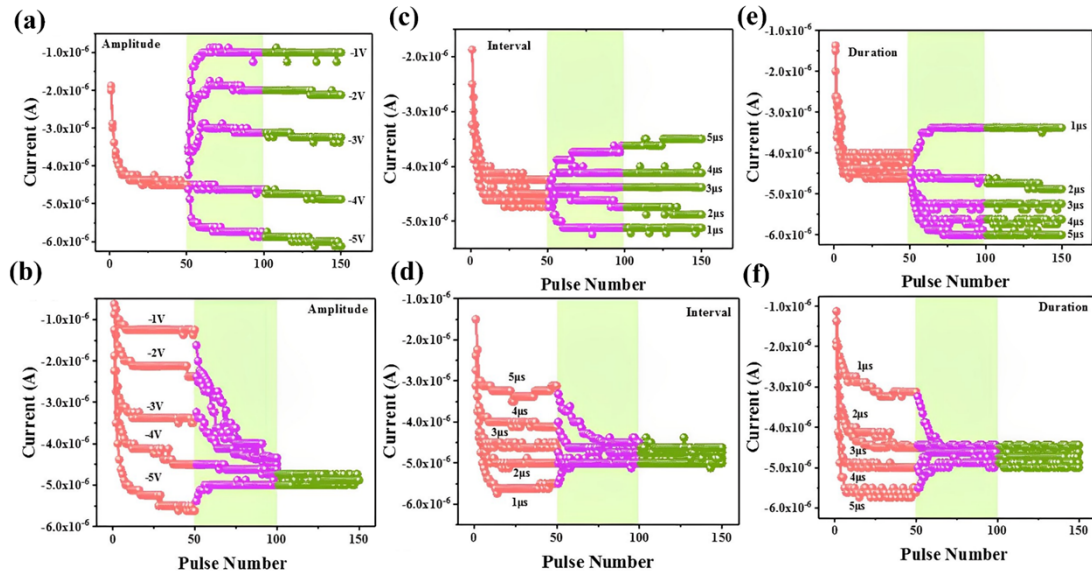Figure S1 The full XPS spectra of the Pd/BLFO/LSMO/STO/Si device.

Figure S2 (a, c, e) We applied 50 fixed pulse trains to the device in stage I, and the pulse parameters were set as follows: pulses with amplitude of -4 V, pulse width and interval of 2 μs. A total of 100 pulse sequences with (a) different amplitudes, (c) different intervals and (e) different pulse widths were applied in Phase II and Phase III. (b, d, f) We applied 100 parameter-invariant stimulation pulses (voltage of -4 V, interval and pulse width were both 2 μs) in stage II and stage III, and 50 stimulation pulses with (b) different amplitudes (d) different intervals and (f) different pulse widths were applied in stage I.

We applied the pulse sequence diagram shown in Supporting Figure S10 to the device and observed the changes in the current of the device under different stimulation pulse modes

(Figure S2). We divided the test results into three stages, and the research results explained the phenomenological model of absolute refractory period and relative refractory period. When the intensity of the first pulse sequence is greater than the intensity of the second pulse sequence, the current of the device decays and is not excited under the second pulse sequence. This can be used to explain the absolute refractory period. When the intensity of the first pulse sequence is less than the intensity of the second pulse sequence, the current of the device increases, which can be used to explain the relative refractory period.[1,2] Among them, stage I is the first 50 pulses of the pulse sequence, and stage II and stage III constitute the last 100 pulses of the pulse sequence. We set the parameters of the 50 sequences of pulses in phase I as follows: amplitude of -4 V, interval and pulse width of 2 µs; In addition, we applied a total of 100 sequence pulses with (a) different amplitudes, (c) different intervals (e) different pulse widths in Phase II and Phase III to study the variation of device current. In Fig. S2 (a), the voltage of the second stage varies from -1 V to -5 V, when the stimulation of the second stage is smaller than that of the first stage (-1 V, -2 V, -3 V), the device current decreased. Conversely, when the stimulation in the second phase was larger than that in the first phase (-5 V), the device current increased. Figure S2 (c) shows that the current of the device is also affected by the interval of the second stage. When the interval of the second stage is larger than that of the first stage (3 µs, 4 µs, 5 µs), the device current decreases; when the interval of the second phase is smaller than that of the first phase (1 µs), the device current increases. When the applied pulse width was increased from 1 µs to 5 µs (Fig. S2 (e)), the following results were observed: when the pulse width of the second stage was larger than that of the first stage (3 µs, 4 µs, 5 µs), the device current increases. Conversely, when the pulse width of the second stage is smaller than that of the first stage (1 µs), the device current decreases.

We applied 100 parameter-invariant stimulation pulses (voltage of -4 V, 2 µs interval and pulse width) in Phase II and Phase III, and 50 sequences of pulses in Phase I with (b) different amplitudes (d) different intervals and (f) different pulse widths to further investigate the subsequent changes in the device current, the results are shown in Fig. S2 (b, d, f). In Fig. S2 (b), when the pulse amplitude of phase I is higher than the subsequent pulse amplitude, the current of the device in phase I is larger than that in phase II and phase III. On the contrary, when the pulse amplitude of phase I is lower than the current in phase II and phase III, the

current of the device in Phase I is smaller than that in Phase II and Phase III. Figure S2 (d, f) show the results of the current changes in the first stage according to different intervals (1 μs to 5 μs) and different pulse widths (1 μs to 5 μs), respectively. When the interval of phase I is greater than the interval of the latter two phases, the current value of phase I is lower than the current value of the latter two phases; when the interval of phase I is smaller than the interval of the latter two phases, the current value of phase I will be higher than the current values of the latter two stages. However, the opposite result to that in Fig. S2 (d) was observed in Fig. S2 (f).
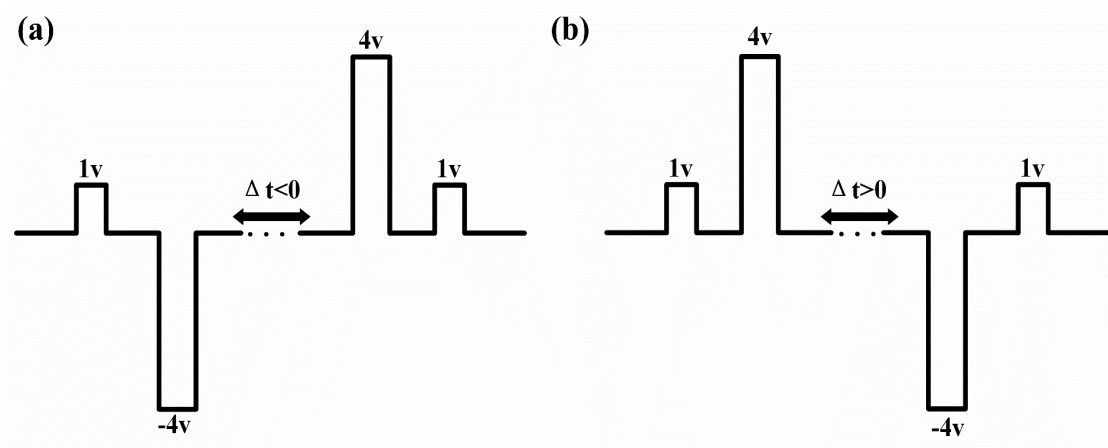

Figure S3 Waveform scheme for spike-timing dependent plasticity (STDP) measurement. Where 1v is the read pulse, 4v is the write pulse, and the width of both the read and write pulses is 5 μs.
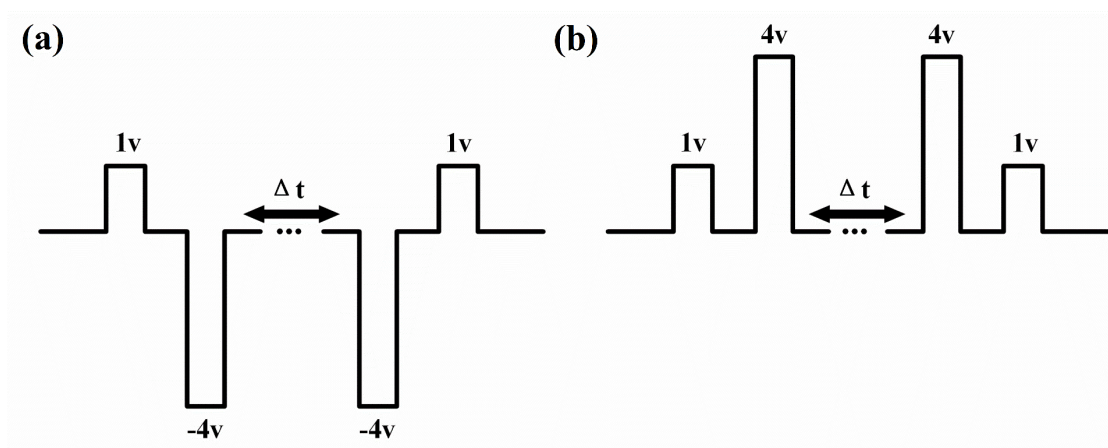

Figure S4 Measurement waveform of paired-pulse facilitation. (a) Negative pulse. (b) Positive pulse. Where 1v is the read pulse and the width of both the read and write pulses is 5 μs.

Table 1. Comparison of the parameters with other ferroelectric memristor devices.

Structure	Film thickness	Leakage Current (0.5 V)	R_{off}/R_{on}	EPSC	PPF	STDP	Ref.
Au/HZO/Si	20 nm	~ $1 \cdot 10^{-6}$A	15	-	Yes	Yes	[3]
BTO/LSMO/STO	300 nm	$2 \cdot 10^{-6}$A	-	-	-	-	[4]
TiN/HZO/Pt	9 nm	-	~5	-	-	Yes	[5]
TiN/HZO/Al$_2$O$_3$/TiN	12 nm	-	14	-	-	Yes	[6]
Al/IGZO/HZO/TiN	24 nm	--	-	-	-	-	[7]
TiN/HZO/TiN	10 nm	-	-	-	-	-	[8]
Pt/Al$_2$O$_3$/HfO$_2$/ HfAlO$_x$/TiN	8 nm	~10^{-5}A	>100	-	Yes	Yes	[9]
n^{++} Si/TiN/HZO/ GeSn/Ni	14.5 nm	-	10	-	Yes	Yes	[10]
Pd/Si:HfO$_2$/LSMO/ STO/Si	6.8 nm	10^{-1}A	176	Yes	Yes	Yes	[11]
Au/Ti/ZnO/BFO/ SRO/BTO/mica	1.2 nm	-	10	-	-	Yes	[12]

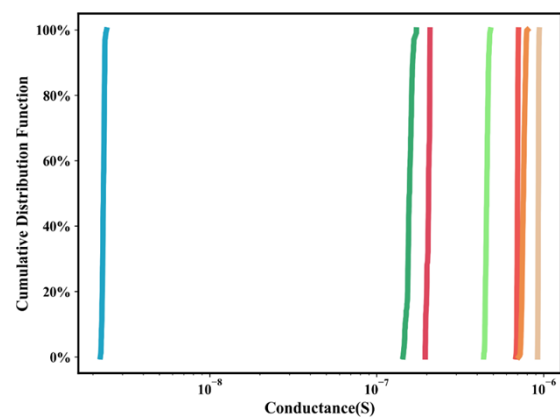|							
Pd/ BLFO/ LSMO/ STO/Si	6.9 nm	$2.5 \cdot 10^{-8}$A	~10^3	Yes	Yes	Yes	This work

Figure S5 Cumulative distribution function of multi-conductance states for LBFO devices.
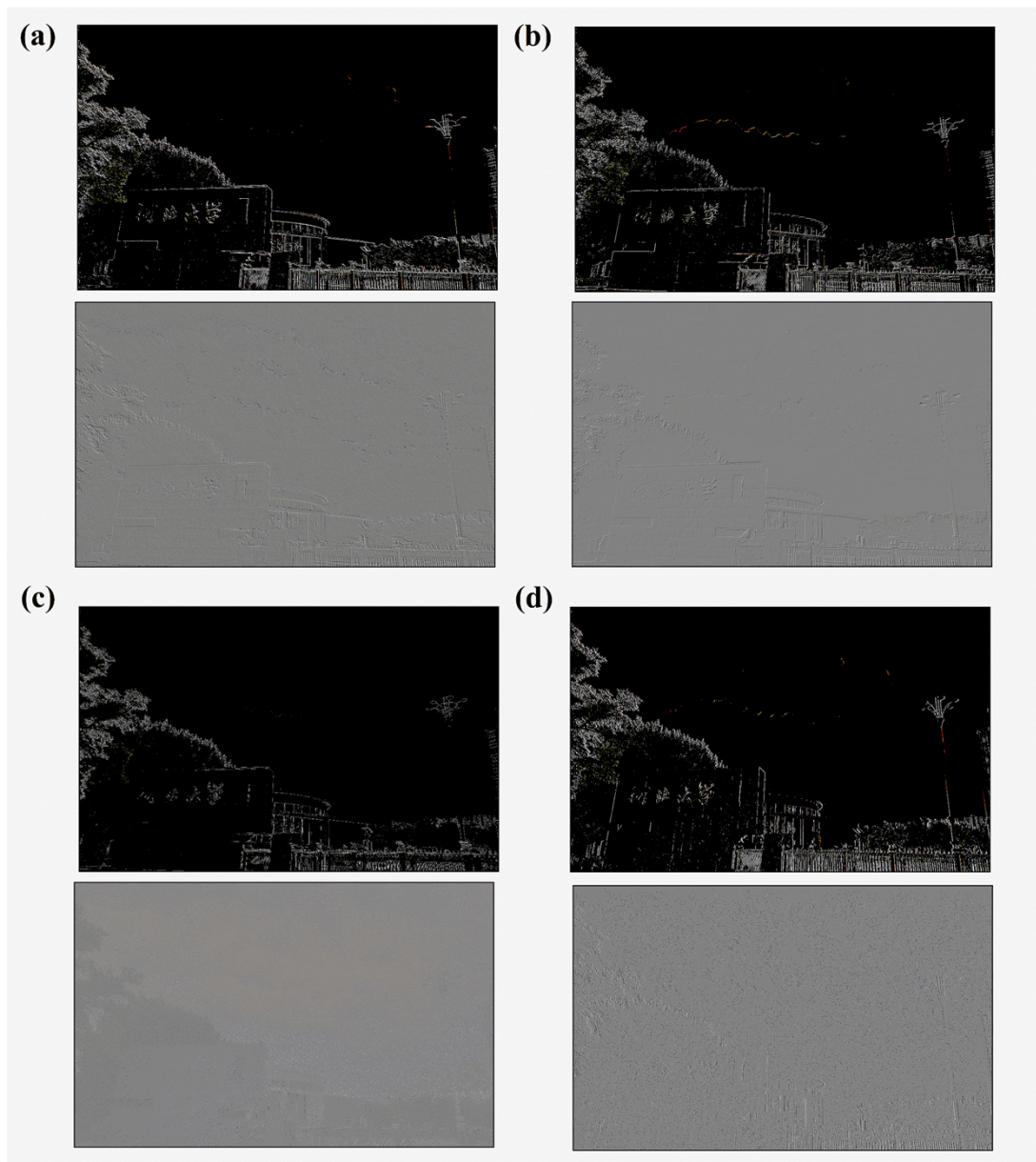
Figure S6 Other convolution kernels process images. (a) Pure software (top) and simulation (bottom) of the Prewitt operator (diagonal) processing the image. (b) Pure software (top) versus simulation (bottom) of the image processed by the Prewitt operator (anti-diagonal). (c) Pure software (top) and simulation (bottom) of the image processed by the Laplace operator (d) Pure software (top) versus simulation (bottom) for edge detection in the vertical direction.
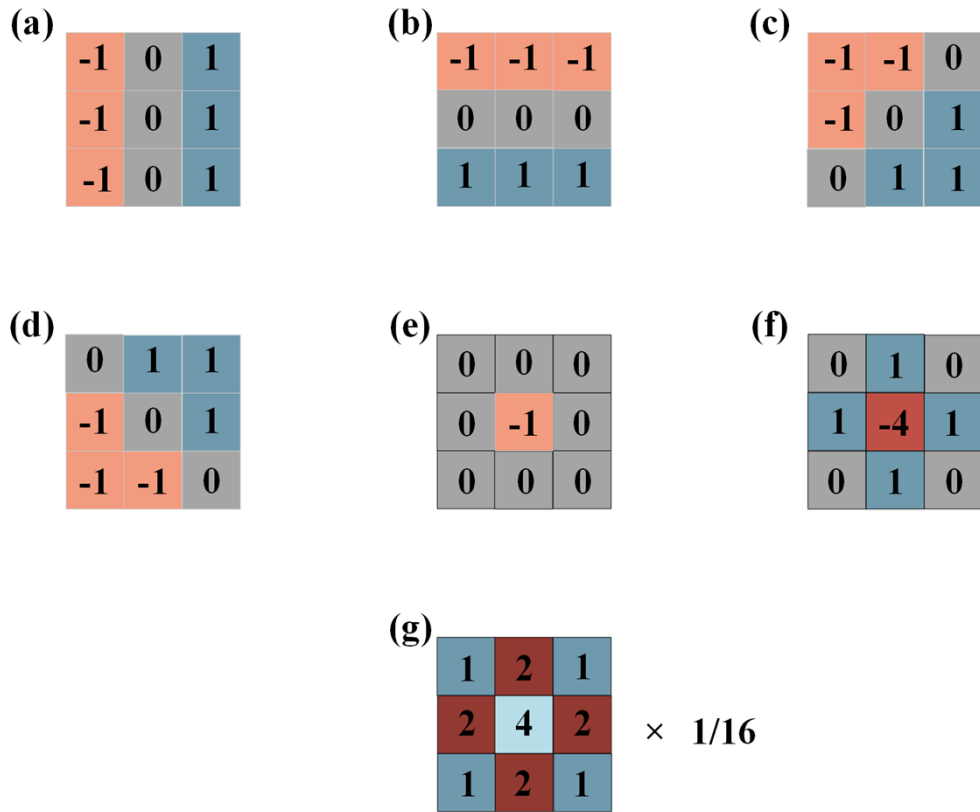
Figure S7 Convolution kernel. (a) Prewitt operator (horizontal). (b) Prewitt operator (vertical). (c) Prewitt operator (antidiagonal). (d) Prewitt operator (diagonal). (e) Flip. (f) Laplacian operator. (g) Gaussian convolution kernel.
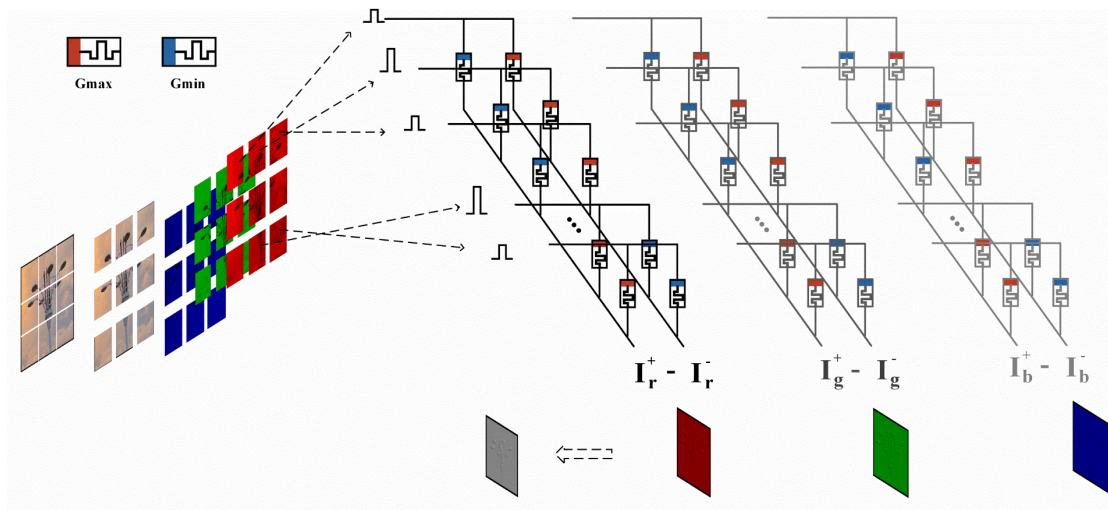

Figure S8 Three-channel convolution process for the same convolution kernel.

As shown in Figure S8, the three channel images will be convolved sequentially, and the convolution kernel will remain unchanged during this process.
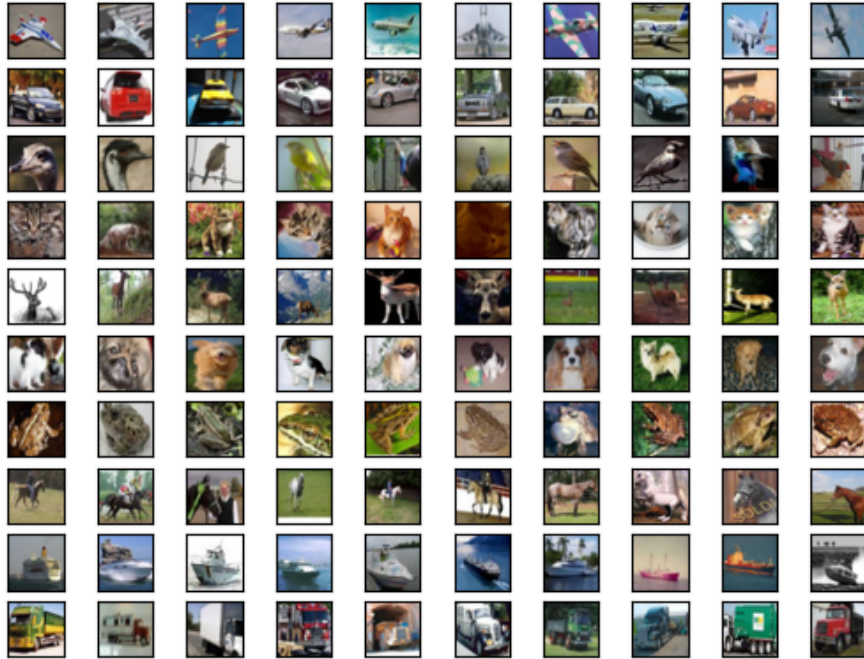
Figure S9 Partial images in the CIFAR-10 dataset.[13]

In the CIFAR-10 dataset, there are ten kinds of color pictures, namely aircraft, cars, birds, cats, deer, dogs, frogs, horses, boats and trucks. 60000 sheets in the dataset 32 × 32 color pictures, including 50000 for training and 10000 for testing.
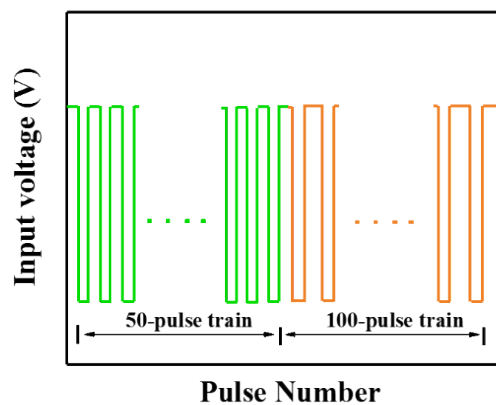

Figure S10 Schematic diagram of pulse sequence applied to the device.

Supplementary Note 1

FTJ devices consist of an ultrathin ferroelectric film with two electrodes, where the inversion of the ferroelectric polarization leads to a change in tunneling resistance. The intrinsic

mechanism of the resistance transition is the change in the potential barrier distribution caused by the switching of the ferroelectric polarization. In addition, the transport mechanisms of FTJ include direct tunneling, Fowler-Nordheim tunneling, and thermionic current.[14, 15]

In order to explore the resistance switching mechanism of the device, we conducted the I-V fitting curve of the device. As shown in Figure S11(a), the thermionic emission (TE) dominates the charge conduction, this is consistent with other study.[15, 16] Considering the thickness of 6.9 nm is also the reason why thermionic emission is more advantageous than Fowler-Nordheim tunneling. Flipping of ferroelectric polarization alters the interface barrier to modulate resistive switching behavior. The Schottky fitting formula is:

$$j_{Schottky} = A^{**}T^2 exp\left[-\frac{1}{k_bT}\left(\Phi_B - \sqrt{\frac{e^3E}{4\pi\varepsilon_0\varepsilon_{ifl}}}\right)\right]$$

(1)

where Φ_B is the potential barrier, A** is the effective Richardson's constant, and ε_{ifl} is the permittivity of the ferroelectric responsible for image force lowering.
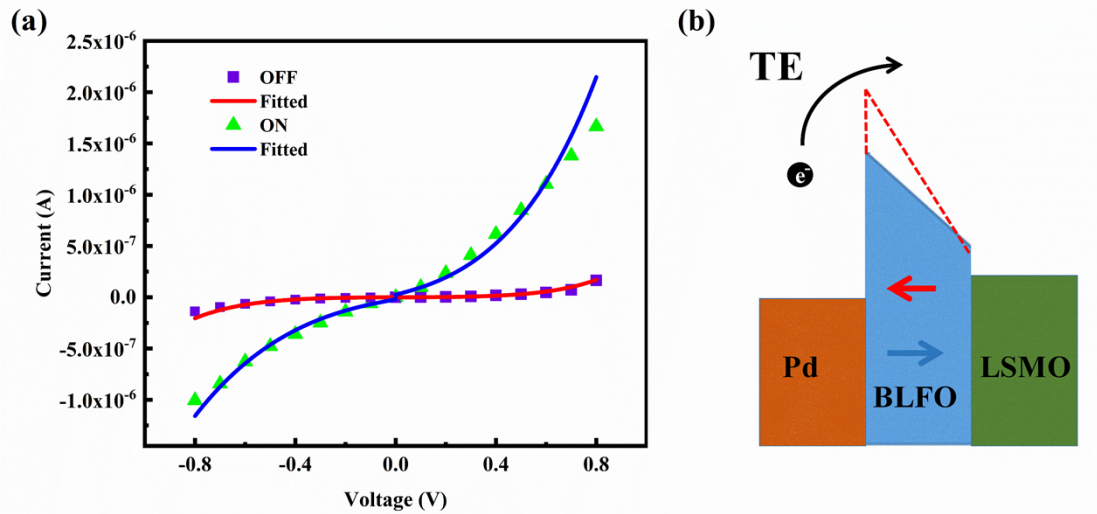

Figure S11 (a) the I-V fitting curve and (b) schematic diagram of the thermionic emission (TE) conduction mechanism

The Figure S11(b) illustrates the expected band diagram of the Pd/BLFO/LSMO/STO/Si device. For the downward polarization case, the oxygen vacancies at the interface would gather on the Pd side and the negative polarization bound charges would gather on the BLFO side, resulting in a built-in electric field pointing from the Pd to BLFO, and the Schottky barrier would decrease and the device would be at LRS.[17] On the contrary, for the upward polarization

case, the Schottky barrier would increase and the device would be at HRS. This is consistent with the results of literature.[18]

Supplementary Note 2

The VGG8 convolutional neural network contains a total of 8 layers. Convolve the three-channel image in the CIFAR-10 dataset with a convolution kernel of size 3×3×3×128 (depth × length × height × batch) to obtain the feature map C1, and pad the image to overcome the boundary effect, so that the size of the output feature map is the same as the size of the input map. Then a 2×2 max-pooling operation is performed on the feature map C1, and the feature map S1 is obtained. Feature map C2 is obtained by convolving S1 with a convolution kernel of size 128×3×3×256. C2 performs a second 2×2 max-pooling operation after the padding operation, resulting in feature map S2. S2 is convolved with a convolution kernel of size 256 × 3 × 3 × 512 to obtain feature map C3, C3 obtains feature map S3 after the same max-pooling operation as the previous two, and the size of S3 is 4 × 4 × 512. After that, S3 is stretched into a vector with 8192 elements. After going through the fully connected layers, the network will output 10 probabilities. Based on the probabilities output by these 10 neurons, we will get the class corresponding to the input image.[19]

Supplementary Note 3

The LTP and LTD characteristics of the devices measured in the experiment are fitted by the following nonlinear weight updating formula.[19, 20]

$$G_{LTP} = B\left(1 - e^{\left(-\frac{P}{A_{LTP}}\right)}\right) + G_{min}$$

$$G_{LTD} = -B\left(1 - e^{\left(\frac{P-P_{max}}{A_{LTD}}\right)}\right) + G_{max}$$

$$B = \left(G_{max} - G_{min}\right)\bigg/\left(1 - e^{\left(-\frac{P_{max}}{A_{LTP,LTD}}\right)}\right)$$

Here, G_{min} and G_{max} represent the maximum and minimum conductance values respectively, P_{max} represents the maximum number of pulses, B is a function of A_{LTP} and A_{LTD}, and A_{LTP} and sA_{LTD} represent the nonlinear factors of enhancement and inhibition respectively.

In the fitting based on LBFO device, A_{LTP}=1.49 and A_{LTD}=1.90. In order to better conform to the characteristics of the device, we set the cycle-to-cycle variation of the device to 0.02, and we added a random number analog noise with a mean value of 0 and a standard deviation of 1.[21] The relevant simulation results are shown in Figure 5 (c).

References

1.   J. Niu, Z. Fang, G. Liu, Z. Zhao and X. Yan, *Science China Materials*, 2023, **66**, 1148-1156.
2.   X. Yan, G. Wang, J. Zhao, Z. Zhou, H. Wang, L. Zhang, J. Wang, X. Li, Y. Pei and C. Qin, *Journal of Materials Chemistry C*, 2020, **8**, 5183-5190.
3.   T. Yu, F. He, J. Zhao, Z. Zhou, J. Chang, J. Chen and X. Yan, *Science China Materials*, 2020, **64**, 727-738.
4.   M. Li, J. Zhou, X. Jing, M. Zeng, S. Wu, J. Gao, Z. Zhang, X. Gao, X. Lu and J. M. Liu, *Advanced Electronic Materials*, 2015, **1**, 1500069.
5.   L. Chen, T.-Y. Wang, Y.-W. Dai, M.-Y. Cha, H. Zhu, Q.-Q. Sun, S.-J. Ding, P. Zhou, L. Chua and D. W. Zhang, *Nanoscale*, 2018, **10**, 15826-15833.
6.   B. Max, M. Hoffmann, H. Mulaosmanovic, S. Slesazeck and T. Mikolajick, *ACS Applied Electronic Materials*, 2020, **2**, 4023-4033.
7.   M.-K. Kim and J.-S. Lee, *Nano Letters*, 2019, **19**, 2044-2050.
8.   S. Oh, T. Kim, M. Kwak, J. Song, J. Woo, S. Jeon, I. K. Yoo and H. Hwang, *IEEE Electron Device Letters*, 2017, **38**, 732-735.
9.   M. Ismail, C. Mahata and S. Kim, *Journal of Alloys and Compounds*, 2022, **892**, 162141.
10.   C.-P. Chou, Y.-X. Lin, Y.-K. Huang, C.-Y. Chan and Y.-H. Wu, *ACS Applied Materials & Interfaces*, 2020, **12**, 1014-1023.
11.   X. Yan, X. Jia, Y. Zhang, S. Shi, L. Wang, Y. Shao, Y. Sun, S. Sun, Z. Zhao and J. Zhao, *Nano Energy*, 2023, **107**, 108091.
12.   H. Sun, Z. Luo, C. Liu, C. Ma, Z. Wang, Y. Yin and X. Li, *Journal of Materiomics*, 2022, **8**, 144-149.
13.   A. Krizhevsky and G. Hinton, 2009.
14.   J. Yoon, S. Hong, Y. W. Song, J.-H. Ahn and S.-E. Ahn, *Applied Physics Letters*, 2019, **115**, 153502.
15.   D. Pantel and M. Alexe, *Physical Review B*, 2010, **82**, 134105.
16.   H. Y. Yoong, H. Wu, J. Zhao, H. Wang, R. Guo, J. Xiao, B. Zhang, P. Yang, S. J. Pennycook and N. Deng, *Advanced Functional Materials*, 2018, **28**, 1806037.
17.   R. Meyer, J. R. Contreras, A. Petraru and H. Kohlstedt, *Integrated Ferroelectrics*, 2004, **64**, 77-88.
18.   L. Feng, S. Yang, Y. Lin, D. Zhang, W. Huang, W. Zhao, Y. Yin, S. Dong and X. Li, *ACS Applied Materials & Interfaces*, 2015, **7**, 26036-26042.

19.   X. F. Lu, Y. Zhang, N. Wang, S. Luo, K. Peng, L. Wang, H. Chen, W. Gao, X. H. Chen, Y. Bao, G. Liang and K. P. Loh, *Nano Letters*, 2021, **21**, 8800-8807.

20.   X. Peng, S. Huang, H. Jiang, A. Lu and S. Yu, *IEEE Transactions on Computer-Aided Design of Integrated Circuits and Systems*, 2021, **40**, 2306-2319.

21.   S. T. Yang, X. Y. Li, T. L. Yu, J. Wang, H. Fang, F. Nie, B. He, L. Zhao, W. M. Lü and S. S. Yan, *Advanced Functional Materials*, 2022, **32**, 2202366.